Article

Physico-Chemical Features of Undoped and Fe/Cu-Doped Na$_{0.67}$MnO$_2$-Layered Cathodes for Sodium Batteries

Marco Ambrosetti [1], Maria Cristina Mozzati [2], Alberto Cini [3,4], Maria Fittipaldi [3,4], Daniele Spada [1], Michela Sturini [1], Irene Quinzeni [5] and Marcella Bini [1,6,*]

[1] Chemistry Department, University of Pavia, Viale Taramelli 16, 27100 Pavia, Italy
[2] Physics Department and CNISM, University of Pavia, via Bassi 6, 27100 Pavia, Italy
[3] INSTM and Department of Physics and Astronomy, University of Florence, via Sansone 1, 50019 Sesto Fiorentino, Italy
[4] INFN Sezione di Firenze, 50019 Firenze, Italy
[5] RSE—Ricerca sul Sistema Energetico, via R. Rubattino 54, 20134 Milano, Italy
[6] National Reference Centre for Electrochemical Energy Storage (GISEL)—INSTM, Via G. Giusti 9, 50121 Firenze, Italy
* Correspondence: bini@unipv.it

Featured Application: The paper's results could be useful in the field of sodium-ion batteries.

Abstract: Na$_{0.67}$MnO$_2$ (NMO) stands out among the layered cathode materials used for sodium batteries due to its high-capacity values, low cost, and environmental friendliness. Unfortunately, many drawbacks arise during cycling, but nanostructure tailoring and doping can help to mitigate them. Our aim was to synthesize undoped and Cu- or Fe-doped NMO samples via the sol-gel route, with a different cooling step to room temperature, i.e., in a natural way or via quenching. The formation of a mixture of polymorphs was observed, as well as differences in the external morphology of the powders' grains. The use of spectroscopic techniques, Mössbauer spectroscopy for the Fe-doped samples and Electron paramagnetic resonance, allowed us to gain insights into the oxidation states of transition metals and to make suggestions about the magnetic ordering, as well as on the possible presence of magnetic impurities. Cyclic voltammetry and galvanostatic cycling results were interpreted on the basis of the spectroscopic data: the introduction of substituents, in general, worsens the capacity values, due to the decrease in the P2 amount and the introduction of structural distortions. The structural stability of the samples in air as a function of time was also analyzed via X-ray diffraction, demonstrating the positive effect of Cu presence.

Keywords: Na$_{0.67}$MnO$_2$; SIBs; XRPD; Mössbauer spectroscopy; EPR spectroscopy; electrochemical measurements

1. Introduction

Sodium-ion batteries (NIBs) are nowadays considered to be the most promising candidate to replace Lithium-ion batteries (LIBs) in the near future, mainly due to the chemical similarity of lithium and sodium ions and the high natural abundance of sodium [1,2]. The main limiting issue for NIBs application is related to their cathode counterpart, which underwent uncontrollable phase transitions and volume changes during repeated charge-discharge cycles, preventing short-term battery commercialization. For this reason, the main efforts of researchers have been devoted to developing high-performance cathodes [3,4]. The most intriguing of the identified materials are the transition layered metal oxides, Na$_x$MO$_2$ (M = Mn, Co, Ni, Fe), due to their high theoretical specific capacity [5]. This is particularly true for Na$_{0.67}$MnO$_2$ (NMO) with a P2-type structure (following the current Delmas notation for this class of materials [6]) and a

capacity of > 175 mAh/g [7]. The P2-type phase, with AA-BB octahedral layer stacking, allows the direct migration of sodium between adjacent prismatic sites, thus enabling rapid Na^+ ions transport and showing better applicability with respect to the O3-type phase. In addition, NMO has low-cost constituting elements and the environmental friendliness of manganese. Unfortunately, some challenges are related to the irreversible structural distortions caused by Mn^{3+} (Jahn-Teller) ions, poor cycling stability due to severe volume changes and mechanical stress during intercalation/deintercalation, and an unsatisfactory energy density limited by the low redox potential of the Mn^{3+}/Mn^{4+} redox couple [5]. Attempts to solve these issues include cation doping or co-doping and nano-structuring, as well as the formation of composites with graphene, strategies used for many other electrode materials [8–18]. As has been well demonstrated in the battery literature, the samples' morphology plays an important role in the electrochemical performances. It was proven that, for layered materials, the performance can be optimized by adjusting the Na/Mn ratio, the sintering temperature, and the cooling rate [13], which at the same time can be useful to control the Mn vacancies that were suggested to form on transition metal layers due to the uptake of oxygen during the cooling process, resulting in an increase in the manganese oxidation state and the formation of manganese-deficient phases [11,19]. It was suggested that the quenching process from high temperatures could avoid the Mn vacancies, stabilizing an orthorhombic P2 form with the *Cmcm* space group [7,10]. However, a high Mn^{3+} amount is still present in the sample, making unavoidable the multiphase transitions during cycling. A clear correlation between the cooling treatment and structure stabilization was not identified, particularly for the doped $Na_{0.67}MnO_2$ samples [11,15]. The doping was suggested to improve the structural stability during sodiation/desodiation and, indeed, the long-term cyclability. One of the most investigated doped compounds is $Na_{0.67}Mn_{0.667}Ni_{0.333}O_2$, with the substitution of 1/3 of the manganese in the original NMO with nickel: in this case, an increase in the redox potential and the improvement of cycling performance have been demonstrated [8]. Starting from this stoichiometry, other compositions were obtained by substituting manganese with variable amounts of Fe, Co, Ti, Al, Mg, and Zn or a combination of them, achieving very complex stoichiometries [9–15]. However, Ni and Co are toxic and expensive elements that should be avoided for the necessary transition toward the next generation of sustainable materials for NIBs. Concerning the other dopants, it seems that divalent cations may enhance the structural stability of the main phase by increasing the oxidation state of manganese and limiting the Jahn-Teller effect related to Mn^{3+} ions. In addition, some of them, such as copper, a harmless element, which is less expensive with respect to Ni, can improve the air/water stability of the P2 phase. It was also proven that the Cu^{2+}/Cu^{3+} redox couple is electrochemically active in P2-type structures [20]. Iron, too, is a cheap and abundant ion, itself possibly contributing to the redox processes and helping to limit the phase transformations [21].

The aim of the present paper was to verify the effect of both doping (with the substitution of manganese with harmless and inexpensive dopant ions) and cooling treatment on the physico-chemical properties of $Na_{0.67}MnO_2$. In particular, we performed a systematic study of the stabilized phases and morphology of undoped and Cu- or Fe-doped $Na_{0.67}MnO_2$ samples synthesized via the sol-gel route, with natural cooling or quenching from high temperature to room temperature. Wide use has been made of X-ray powder diffraction, with Rietveld structural refinements and the employment of Scanning electron microscopy with Energy-dispersive spectroscopy. The Mössbauer (for Fe-doped samples) and Electron paramagnetic resonance spectroscopies allowed us to determine the oxidation states of transition metal ions and the possible presence of magnetic impurities. The structural stability of the samples in the air was studied by X-ray powder diffraction. Preliminary cyclic voltammetry and charge-discharge measurements were performed to evaluate the effect of doping on capacity values and capacity retention; the results were discussed and interpreted on the basis of the structural and spectroscopic findings.

2. Materials and Methods

2.1. Synthesis

$Na_{0.67}Mn_{1-x}M_xO_2$ (M=Cu, Fe; x = 0 or 0.2) samples were synthesized via the sol-gel method, with two different cooling thermal treatments of slow cooling or quenching.

$(CH_3COO)Na$ (Merck, ACS grade), $(CH_3COO)_2Mn\ 4H_2O$ (Sigma-Aldrich, > 99%), and $(CH_3COO)_2Cu\ H_2O$ (Merck, ACS grade) or $(CH_3COO)_2Fe$ (Sigma-Aldrich, 95%), were weighed in the proper amounts (Na:Mn:M = 0.67:1−x:x; x = 0 or 0.2) and dissolved in about 100 mL of distilled water, together with citric acid (2:1 moles ratio with respect to the sum of the reagents). In order to compensate for the possible loss of sodium due to the annealing process, a 10 wt % excess (with respect to 0.67 moles of Na) of sodium acetate was added during the synthesis. The solution was stirred, heated to 65 °C, and maintained overnight until all the solvent had evaporated. The obtained white powder was heat-treated in an oven at 350 °C for 5 h to remove the organic component. Afterward, the powder was ground, pelletized, and heat-treated at 800 °C for 12 h following two different cooling treatments: in the first one, the pellets were allowed to slowly cool to room temperature in the oven and in the second one, the pellets were quenched via rapid extraction from the oven. The pellets were ground down and the resulting powders were preserved in a glovebox to avoid contact with the atmosphere until their subsequent use. A portion of the powders was also maintained in air for the structural stability study. In the following sections, the $Na_{0.67}MnO_2$, $Na_{0.67}Mn_{0.8}Cu_{0.2}O_2$, and $Na_{0.67}Mn_{0.8}Fe_{0.2}O_2$ samples will be named NMO, Cu02, and Fe02 for slowly cooled samples, with the same acronyms followed by Q for the quenched samples.

2.2. Instruments

X-ray powder diffraction (XRPD) measurements were performed using a Bruker D5005 diffractometer (Karlsruhe, Germany) with CuKα radiation (40 kV, 40 mA), graphite monochromator, and scintillation detector. The patterns were collected in the angular range of 10–120°, with a step size of 0.03° and a counting time of 12 s per step in a silicon sample holder with low background. Rietveld structural and profile refinement was carried out by means of TOPAS 3.0 Bruker software [22], on the basis of the known crystal structure models of the layered polymorphs. During the refinement, the background coefficients, scale factor, zero or displacement error, lattice parameters, crystallite sizes, isotropic thermal factors, and atomic positions were varied. The occupancies of sodium and dopant ions were fixed to stoichiometric values, due to the complexity of the samples and to the similar X-ray scattering factors of Mn, Cu, and Fe ions. To evaluate the structural stability, the patterns were also collected on all the samples in the 10–70° 2θ range, step 0.03° and 2s/step of counting time after 7, 14, and 30 days of the maintenance in air.

A Tescan Mira 3 (Tescan USA Inc., Warrendale, PA, USA) scanning electron microscope (SEM) was used for the morphological study on gold-sputtered powder samples. Energy-dispersive X-ray spectroscopy (EDS) analysis was also performed with the same instrument on non-sputtered powder samples.

Element measurements were performed via inductively coupled plasma optical emission spectroscopy (ICP-OES iCAP 7400, Thermo Fisher Scientific, Waltham, MA USA) equipped with a concentric nebulizer, cyclonic spray chamber, and ceramic torch, according to the operating conditions suggested by the manufacturer. The linearity range of intensity vs. concentration was obtained using standard solutions (1–10 mg/L) prepared from a 1 mg/mL stock solution. Small amounts, exactly weighted, of each sample were treated with 0.5 mL of ultrapure 65% HNO_3 and 1.5 mL of ultrapure 37% HCl, refluxed for 10 min, evaporated to a small volume, and then diluted to 50 mL with ultrapure water. Clear solutions were obtained and analyzed for the determination of element content.

The Mössbauer measurements were performed by means of a standard Mössbauer setup (home assembled) in transmission geometry. The spectra were collected by means

of a Kr-CO_2 proportional counter, Fast™ (LND Inc., New York, USA) electronics for gamma-ray spectroscopy, and a Wissel™ spectrometer (Blieskastel, Germany), which was run in sinusoidal acceleration mode (v_{max} = 4.0 mm/s) and calibrated using a standard metal iron foil. The γ-ray source was a 25-mCi ^{57}Co in rhodium matrix with the Lamb-Mössbauer factor f = 0.63, as measured by applying the method described by Spina and Lantieri [23]. Approximately 33 mg/cm^2 of each compound was used for the measurements. The Mössbauer spectra were interpreted by means of a fitting procedure, based on the evaluation of the transmission integral function, which takes into account the dependence of the Mössbauer spectra on the sample's effective thickness. The complete expression used to fit the spectra was:

$$Y(v) = N_b(v)\left\{1 - f_S^r \int_{-\infty}^{\infty} L_S(\omega - v, \Gamma_S)[1 - e^{(-t_a\sigma(\omega))}]d\omega\right\}$$

where $Y(v)$ and $N_b(v)$ are the detected counts and the spectrum baseline, respectively, as a function of the transducer velocity v [24]. Moreover, f_S^r is the reduced recoilless fraction of the source and $L_S(\omega - v, \Gamma_S)$ is the Voigt distribution (having v and Γ_S as center and FWHM, respectively) used to describe the source line shape. The Voigt profile has a Lorentzian component with natural line width, while that of the Gaussian one is suitable to reproduce the total linewidth of the source provided by the manufacturer (Γ_S = 0.114 mm/s). Finally, $\sigma(\omega)$ is the absorption cross-section of the sample as a function of the energy ω, expressed in mm/s, and t_a is the effective thickness of the sample. In the limit of "thin absorption approximation" (t_a < 1), each contribution to $\sigma(\omega)$ is expressed as a Voigt doublet, having a Lorentzian component with the natural line width (Γ_n) and a Gaussian one with a broadening σ, describing a particular distribution of hyperfine parameters [25]. Consequently, the total linewidth of each contribution is approximately given by $\Gamma_{tot} = \Gamma_S + \Gamma_n + \sigma$. For both samples, a rather good agreement between experimental and best-fit data was obtained with $\chi^2 \sim 1200$ for the 512 points.

Electron paramagnetic resonance (EPR) measurements have been performed at about 9.46 GHz with a Bruker spectrometer (Karlsruhe, Germany). Particular care has been devoted to determining sample mass and position in the resonant cavity for the comparison of signal intensities (areas). The temperature dependence of the spectra has been investigated in the range of 115–370 K.

The slurries for the electrochemical measurements were prepared by mixing the active materials with carbon (Super C65) and PVdF binder (Solef 5130) at a weight ratio of 80:10:10 in N-methyl-2-pyrrolidone (NMP) (Sigma-Aldrich) and magnetically stirred for about one hour. Afterward, the slurries were coated onto an aluminum foil using a homemade doctor blade, maintained at room temperature until dried, heat-treated at 80 °C overnight in a vacuum oven, then hot-pressed at 200 psi at 100 °C for 5 min. The slurries were maintained in a glove box (MBraun, Garching bei München, Germany, O_2 < 1 ppm, H_2O < 1 ppm) with an Ar atmosphere to avoid contact with moisture.

The electrodes were cut in the form of discs (1 cm in diameter) with a mass loading of about 3 mg/cm^2. Swagelok cells were assembled in the glove box, with the slurries acting as the working electrode, Na metal as the reference and counter electrode, and a Whatman GF/A disc as the separator. The chosen electrolyte was 1 M $NaPF_6$ in EC:DEC (1:1 wt %).

Cyclic voltammetry (CV) was performed by using an Autolab PGSTAT30 (Eco Chemie, Metrohm, Utrecht, The Netherlands) at a scan rate of 0.1 mV/s for five cycles in the potential range of 1.7–4.4 V. For galvanostatic charge–discharge tests, the Swagelok cells were cycled on a Neware (Hong-Kong, China) battery tester in the same potential range for 10 cycles at C-rates of between C/5 and 5C, after a conditioning cycle at C/20 and C/10.

3. Results

3.1. Structural and Morphological Results

In Figure 1, the XRPD patterns of undoped and doped samples obtained from slow cooling (A) and quenching (B) are reported.
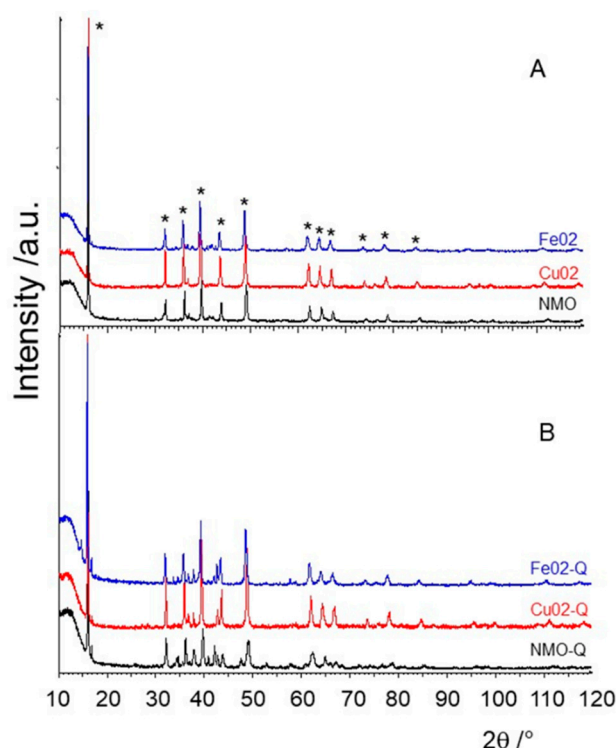

Figure 1. XRPD patterns of the samples obtained from the slow cooling (**A**) and quenching (**B**) processes. The stars mark the main reflections of P2 polymorph (valid for both (**A**,**B**) panels).

The patterns of slowly cooled samples are similar: for all of them, the main peaks can be assigned to the P2 phase (Figure 1A, stars) as expected, due to their stoichiometry [11,13]. However, after a more careful observation, the peaks of all the patterns appear asymmetric or broadened: this is compatible with the stabilization of a distorted form of P2 polymorph with monoclinic symmetry, which will be indicated as P'2, together with the main P2 phase. Low peaks, particularly evident in the 30–45° 2θ range, can be detected, probably due to secondary phases, apart from Cu02. The quenching process introduced visible differences in the patterns, particularly for the NMO-Q sample (Figure 1B): a higher number of peaks is evident with respect to NMO, while the quenched doped samples more closely resemble their slowly cooled analogs [11]. The effect of the cooling step on the phase's stabilization has also been studied in the literature. It was reported that slow cooling preserves the P2 phase (with manganese vacancies on the transition metal octahedral layers, due to oxygen uptake), while quenching avoids the vacancy formation and allows the stabilization of the orthorhombic *Cmcm* phase [7,11,26].

The type and amount of the stabilized phases, as well as their main structural parameters, were determined by Rietveld structural refinement of all the patterns, using the TOPAS 3.0 software [22]. The results are reported in Table 1; as an example, in Figure S1 in the Supplementary Materials, the graphical comparisons between the experimental and calculated patterns of Cu02 and Cu02-Q samples are shown. A good agreement was found, as evident from the difference curve, suggesting reliable results; this was also demonstrated by the agreement indices of all the refinements (Table 1). In the case of the main peak at about 16°, suffering the preferred orientation effect, a small residual is detectable (Figure S1).

Table 1. Main structural parameters, secondary phase amounts, and agreement indices (R_{wp} and GoF) obtained from Rietveld refinements on undoped and doped sample patterns from both the slow-cooling and quenching processes.

	NMO	Cu02	Fe02	Cu02-Q	Fe02-Q	NMO-Q
			P2			***Cmcm***
Lattice parameters (Å)	2.8700 (1) 11.1306 (7)	2.8857 (1) 11.1536 (5)	2.8960 (1) 11.1844 (10)	2.8980 (1) 11.1806 (8)	2.9117 (1) 11.2487 (10)	2.8358 (3) 5.2561 (5) 11.2151 (15)
Volume (Å³)	79.4	80.4	81.2	81.3	82.6	167.2
Cry. size (nm)	78 (1)	105 (2)	84 (1)	101 (2)	87 (2)	70 (2)
			P'2			**P'2**
Lattice parameters (Å)	2.7853 (11) 4.9738 (21) 11.2651 (30) 91.61 (3)	2.8810 (4) 5.0115 (8) 11.1648 (13) 90.58 (1)	2.8882 (6) 5.0233 (9) 11.2101 (19) 90.55 (1)	2.8892 (4) 5.0346 (6) 11.2005 (12) 90.39 (1)	2.9056 (6) 5.0765 (8) 11.2383 (18) 90.42 (2)	2.8864 (5) 4.9743 (12) 11.1984 (22) 90.76 (2)
Volume (Å³)	156	161.2	162.6	162.9	165.8	160.8
Crystallite size (nm)	40 (2)	70 (1)	40 (2)	59 (3)	43 (2)	38 (2)
Main phases ratio	6.5	2.8	2.4	1.6	1.7	2.8
Secondary phases (types and total weight %)	O2 O3 5 wt %	-	O1 O2 O3 4 wt%	O1 O2 4 wt %	O1 O2 O3 8 wt %	O1 O2 O3 20 wt %
R_{wp}/GoF	11.08/1.53	8.07/1.53	12.40/1.62	8.01/1.39	11.9/1.54	13.57/1.65

The P2 and monoclinic P'2 polymorphs [11] represent the main phases for all the samples, apart from NMO-Q, which instead contains the *Cmcm* polymorph as the main phase. The weight percentage ratio of the main phases P2 (or *Cmcm*) and P'2 (see Table 1) decreases, passing from NMO to the doped samples, suggesting, for these last ones, the presence of a higher amount of P'2 phase. For the quenched samples the ratios further decrease with respect to the slowly cooled samples but maintain the same trend [7,11]. Apart from the Cu02 sample, constituted by only the P2 and P'2 phases, for all the others, variable amounts of O-type phases were detected, which mainly explains the peaks in the 30–45° angular range (Figure 1). For the slowly cooled samples, the total percentage of O-type polymorphs was low, while it increased in the Fe02-Q and increased markedly in the NMO-Q samples.

Differences in the lattice parameters of the P2 phase and, therefore, in the cell volumes were found between the NMO and doped samples: the volume was slightly higher for the Fe-doped samples, for both slowly cooled and quenched samples. In particular, the *c* parameter increased, passing from the NMO to Cu- and Fe-substituted samples, with a marked increase for Fe02-Q. The crystallite sizes of P2 and P'2 were similar, independently of the doping, while those of P'2 were smaller than those of P2. The Cu-doped samples instead had larger crystallite sizes for both polymorphs.

One aspect that could affect the storage capacity of electrode materials is the structural stability in air. For all the samples, XRPD patterns after 7, 14, and 30 days of maintenance in air after the synthesis were collected: the results are shown in Figures S2–S4 in the Supplementary Materials. NMO (Figure S2A) was slightly degraded: the main P2 phase maintained good crystallinity, but after only 7 days and up to 30 days, Na^+/H_3O^+ exchange or H_2O insertion takes place (as suggested by the presence of two peaks at about 12 and 25°) [27]. The NMO-Q sample showed a marked decrease in peak intensities with time and only after 30 days, a small peak at about 12° was seen (Figure S2B). We should, however, take into consideration that its main phase is represented by the *Cmcm* polymorph, which is different from NMO.

The Cu-doped samples (Figure S3A,B) were stable: only in the case of Cu02, a very small peak at about 12° was evidenced starting from 7 days, while Cu02-Q did not show hydrated phases in all the analyzed range of time. The peak intensities of the P2 phase did not change with time in Cu02, while they slightly decreased in Cu02-Q. It is different in the case of Fe-doped samples (Figure S4): in Fe02, the hydrated phase started to form after 14 days and increased after 30 days (Figure S4A), while the intensities of the main phase slightly decreased. Fe02-Q heavily degraded only after 30 days, with a loss of crystallinity of the main P2 phase and the formation of a large amount of hydrated phase (Figure S4B).

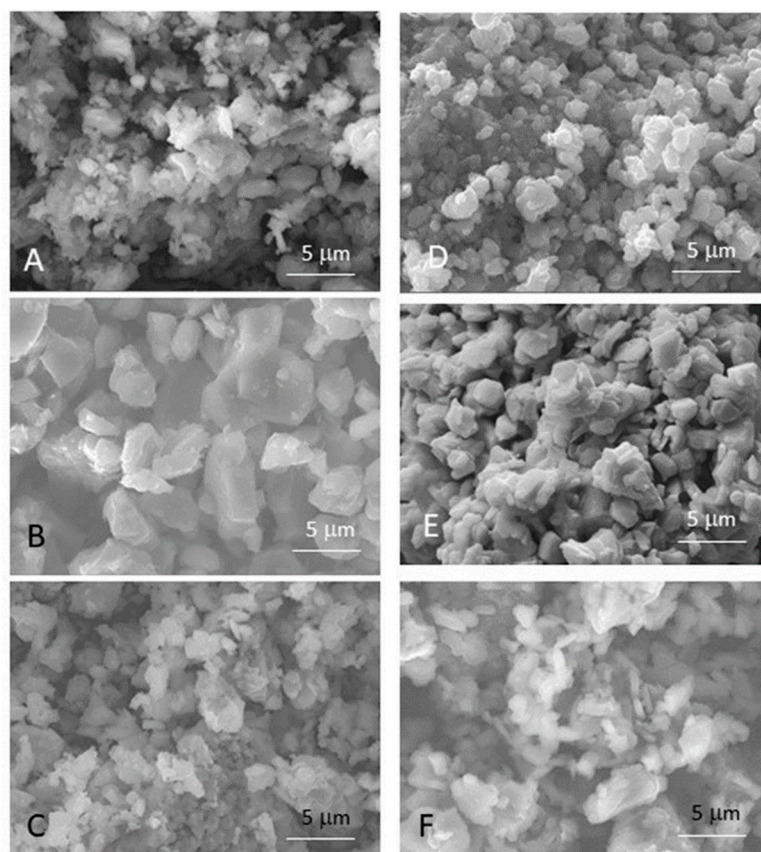The samples' morphology was analyzed via SEM measurements (Figure 2).

Figure 2. SEM images of slowly cooled (**A–C**) and quenched (**D–F**) NMO, Cu02, and Fe02 samples (from top to bottom).

NMO (Figure 2A) and Fe02 (Figure 2C) share a similar form of grains: aggregates of particles with clear edges and sizes up to 3–4 μm can be identified. Some flat particles, with plate-like forms, were also present. The Cu-doped sample morphology (Figure 2B) is different, showing larger particles that are bigger than 5 μm, with blunt edges. The quenched samples were morphologically different (Figure 2D–F). NMO-Q was constituted by aggregates of rounded particles with low porosity, while Fe02-Q showed both rounded and plate-like particles, which are also clearly evident in Cu02-Q, even if they are fused together and have extended dimensions and hexagonal forms. Therefore, both the doping and cooling steps had an obvious effect on the external appearance of the material.

The chemical composition of the samples was determined by means of EDS micro-analysis (Table 2): the obtained formulas were reported together with the Na/Mn ratios and were compared with the stoichiometric ones.

Table 2. Chemical compositions from the EDS analysis for all the synthesized samples.

Samples	Na/Mn Stoichiometric	Na/Mn from EDS	EDS Composition
NMO	0.74	0.78	$Na_{0.77}Mn_{0.98}O_2$
Cu02	0.925	0.925	$Na_{0.74}Mn_{0.80}Cu_{0.20}O_2$
Fe02	0.925	0.88	$Na_{0.73}Mn_{0.83}Fe_{0.17}O_2$
NMO-Q	0.74	0.75	$Na_{0.75}Mn_1O_2$
Cu02-Q	0.925	0.89	$Na_{0.73}Mn_{0.82}Cu_{0.20}O_2$
Fe02-Q	0.925	0.90	$Na_{0.72}Mn_{0.80}Fe_{0.20}O_2$

The EDS compositions were in quite good agreement with the expected stoichiometries. To further verify the reliability of these results, the chemical compositions of slowly cooled samples were also determined with the ICP analysis, a more sensitive analytical technique, which confirmed that the sample stoichiometries (Table S1 in the Supplementary Materials) were in good agreement with the EDS results.

3.2. Mössbauer Spectroscopy

The room-temperature Mössbauer spectra of the Fe-doped samples are shown in Figure 3, together with the corresponding fits.
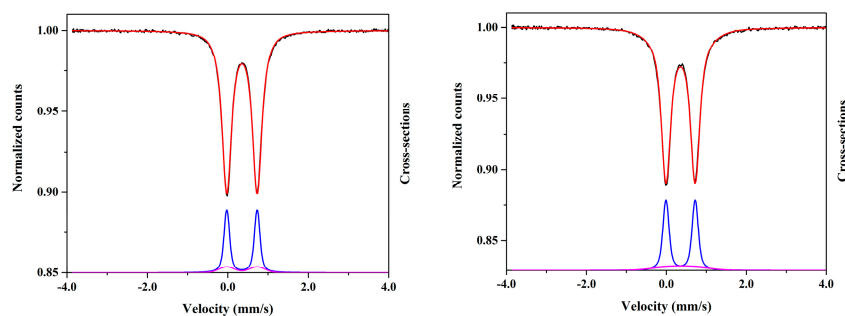

Figure 3. Mössbauer spectra of the Fe02 (**right**) and Fe02-Q (**left**) samples acquired at 293 K (black line) and the corresponding fit (red line). The absorption cross-section of each contribution is also shown.

The parameters extracted from the fit procedure of each sub-spectrum are reported in Table 3, together with the relative weight calculated from the values of the effective thickness.

Table 3. The ^{57}Fe Mössbauer parameters, extracted from the fit of the spectra: isomer shift with respect to α-Fe (δ) and quadrupole splitting (Δ). Parameters with no errors were kept fixed in the fitting procedure. The relative weight of each contribution is also reported.

Sample	Site	δ (mm/s)	Δ (mm/s)	σ (mm/s)	%
Fe02	1	0.3521 (4)	0.7550 (5)	0.044 (2)	82 (2)
	2	0.3521	0.7550	0.17 (1)	18 (2)
Fe02-Q	1	0.3558 (3)	0.7305 (5)	0.0517 (7)	84.3 (3)
	2	0.3558	0.7305	0.40 (1)	15.7 (4)

The Mössbauer spectra of the two samples were very similar and can both be described by two doublets (namely, site 1 and site 2), one of which (site 1) is clearly prevailing. The isomer shift had approximately the same value for all the sub-spectra, i.e., about 0.35 mm/s, a value associated with Fe^{3+} ions. Moreover, a similar value of the quadrupole splitting was found for both samples. However, the two sites showed a different value for the Gaussian broadening, indicating the presence of a distribution of hyperfine parameters; in particular, site 2 had a broader distribution. Consequently, the quadrupole splitting of all the sub-spectra of both samples can be considered consistent between them. The quadrupole splitting provides information about bond properties and

the local symmetry of the Fe site [28] and can suggest the degree of distortion from the ideal octahedral coordination. The obtained values corroborated the suggestion of the octahedral coordination of Fe^{3+}, as expected for the transition metals located on the layers, and were in good agreement with the literature values of similar samples [21,29].

These results can suggest that due to the presence of only one crystallographic site for the transition metal in both P2 and P'2 lattices, the iron ions were distributed in both the layered structures, with a preference toward the more regular sites of the P2 phase.

3.3. EPR

In Figure 4a,b, the room-temperature EPR spectra for the slowly cooled and quenched samples were reported. All the measurements have been performed using the same experimental conditions; signal intensity always referred to the mass unit of the samples for the sake of comparison.
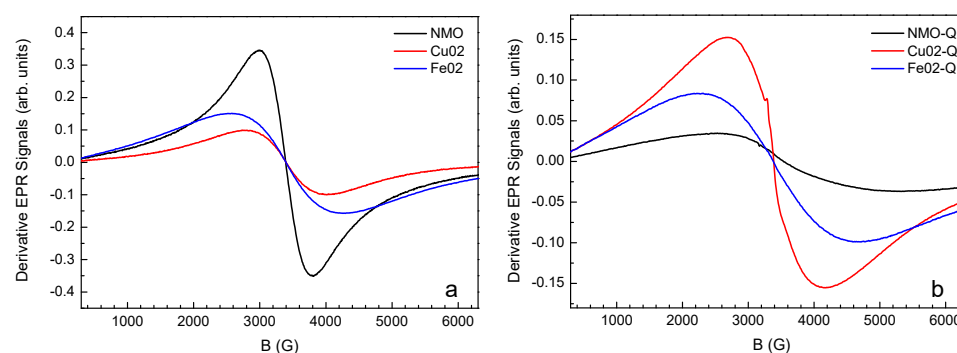

Figure 4. Room-temperature EPR spectra for (**a**) slowly cooled and (**b**) quenched samples.

All the spectra appeared to be composed of or dominated by a broad signal. The spectra of NMO, Cu02, and Fe02 (Figure 4a) were centered at the same g-value (1.991(1)). The undoped sample showed the narrowest line (about 800 G). An analysis of this spectrum disclosed the presence of two overwhelmed contributions: a main, narrower Lorentzian signal that was 750 G wide, and a secondary broader component with a Gaussian character and a linewidth of about 2500 G. Taking into account the data from Table 1 and according to the literature [26], the main signal is ascribable to the P2 phase, while the broader secondary component could be the result of contributions from other phases in the sample (P'2 and O phases). Indeed, after doping, line broadening was observed with respect to the NMO signal, correspondingly to the decrease in the P2 amount and to the overall increase in the other phases (see Table 1). Moreover, for Fe02, clear changes in the extreme parts of the line shape were also revealed. It should be noted that this sample contained the highest overall amount of P'2 and secondary different *O* phases, which then seem to play a role in affecting EPR line width and line shape.

For this series of samples, the signal intensity (area) strongly decreased after Cu doping. This is quite unexpected because Cu/Mn substitution, as well as Fe/Mn substitution, should not lead to a decrease in the amount of Mn^{4+} (see Table 2), Mn^{4+} being the main component responsible for the EPR signal in these compounds. Moreover, the dopants themselves could make a contribution to the EPR spectrum, as both Cu^{2+} and Fe^{3+} are EPR-active ions.

For the quenched samples (Figure 4b), a strongly different situation occurred, confirming the crucial role of annealing in affecting the structural and compositional features of these compounds. In this case, the spectra were centered at different g-values, with a line width that is much broader than that of the slowly cooled samples with the same composition. In particular, the broadest line pertains to NMO-Q ($\Delta B \cong 2700G$), which is also centered at the lowest detected g-value (1.919) among all the investigated samples. This value is then the farthest from g = 1.996, that is, the expected value for Mn^{4+} when

present as a unique magnetic ion in the sample [30]. Besides this, NMO-Q also showed the lowest signal intensity among all the investigated samples. According to the EPR results obtained for the slowly cooled samples, the EPR features achieved for NMO-Q perfectly agreed with the compositional data reported in Table 1 and in the literature [26]: both the *Cmcm* orthorhombic phase and the P'2 and O phases are expected to give rise to different broad contributions to the spectra. Moreover, the markedly different g-value with respect to the one observed for all the other samples can be ascribed to *Cmcm*, which was present as the main phase in the sample, and to the high value of the Mn^{3+}/Mn^{4+} ratio, as also indicated by the EDS results (Table 2). Indeed, the broadest EPR signal observed in the literature for these compounds was related to the presence of Mn^{3+}-Mn^{4+} couples, which led to the development of strong antiferromagnetic interactions, giving rise to a progressive line broadening by lowering the temperature [26]. It is worth noting that among our samples, the highest signal intensity pertains to NMO (about 3 times higher than the one achieved by NMO-Q). A high intensity of the EPR signal is consistent with the presence of a large number of Mn^{4+} ions, in environments mainly containing Mn^{4+} ions or Mn-vacancies (see [26] and the references therein). The Mn-vacancies formation in Mn-O layers was related to oxygen uptake, favored by the slow cooling of the samples, as indeed occurred for NMO. However, the g-value detected for NMO (1.991), which was still different from the expected 1.996 value, was matched with the presence of a certain amount of Mn^{3+} ions coexisting with the Mn^{4+} and Mn-vacancies.

For the quenched series, the doping led to line-narrowing with respect to NMO-Q, consistently with the presence of the P2 polymorph as the main phase instead of the orthorhombic *Cmcm* polymorph in NMO-Q. In particular, the narrower line was observed for Cu02-Q, for which a g-value very near to the expected 1.996 was also detected, together with an important increase in signal intensity with respect to NMO-Q. For Fe02-Q, the presence of a greater number and variety of the O phases again seems to play a role in affecting the features of the EPR spectrum. Besides this, in this case, the spectrum was centered at $g \cong 2$, suggesting a non-negligible contribution to the spectrum by Fe^{3+} ions.

From the EPR results, it can be inferred that the doping seems to play a contrasting role against the annealing procedure, reducing the differences between samples with the same composition with respect to the undoped samples, looking, in particular, at the line width values.

This was evident in Figure 5, where the line width values as a function of temperature were compared for all the samples.
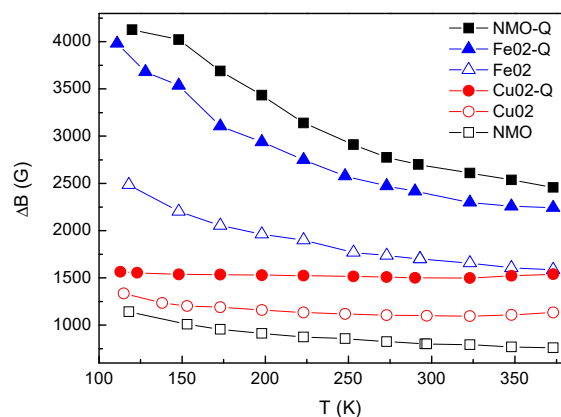

Figure 5. EPR linewidth values as a function of temperature for all the samples.

This picture also evidenced the wider line widths for the Q-sample with respect to its analogous slowly cooled sample. Besides this, the increase in ΔB value by decreasing the temperature confirmed that magnetic correlations occurred in these samples, which is in agreement with the findings reported in the literature [26].

The peculiar behavior of NMO-Q is clearly evidenced in Figure 6, where the temperature dependence of the g-factor for all the samples is shown.
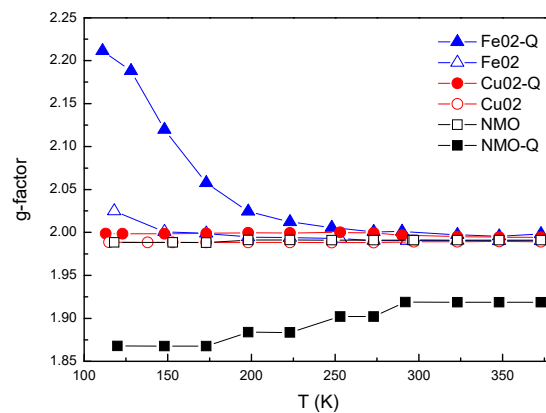

Figure 6. The g-factor as a function of temperature for all the samples.

It can also be observed that the g-factor holds a nearly constant value in the whole investigated temperature range for all the samples but for Fe02-Q, for which an increase was detected by decreasing the temperature. This is possibly related to the low amount of Mn vacancies, as a consequence of quenching, with respect to the analogous slowly cooled sample (Fe02).

Useful indications can be drawn from the temperature dependence of the signal intensity (area), as reported in Figure 7 for all the investigated samples: vertically, a comparison can be made between those samples obtained via the same annealing procedure and with different compositions, while horizontally, samples with the same composition but obtained after different annealing treatments can be compared.
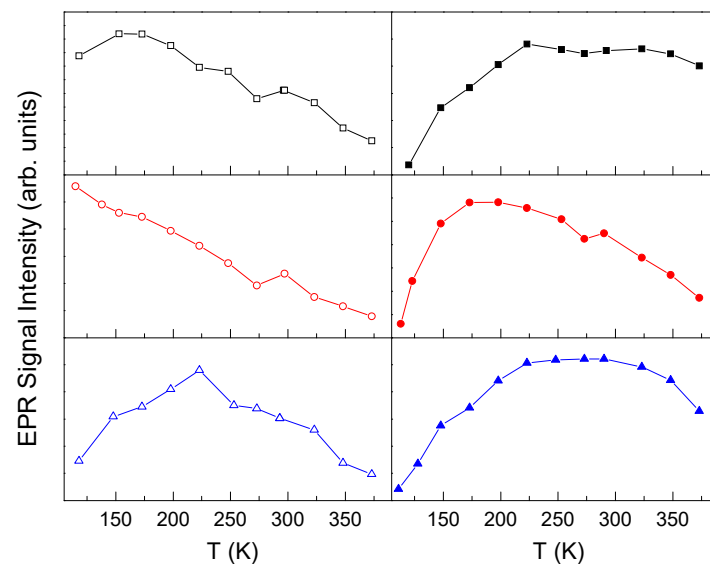

Figure 7. The trend of signal intensity (area) for slowly cooled (left column) and quenched (right column) samples vs. temperature. Black, red, and blue symbols represent undoped, Cu-doped, and Fe-doped samples, respectively.

These trends suggested that the stronger correlations concern the Q-samples with respect to the slowly cooled ones, correspondingly to the presence of a greater number of Mn^{3+}-Mn^{4+} couples. Besides this, in each series of samples, Cu-doping seems to favor a

paramagnetic-like behavior, while Fe-doping tends to support the onset of magnetic correlations.

3.4. Electrochemical Results

The sodium storage properties of layered cathodes were evaluated in a half-cell configuration. Cyclic voltammetry (CV) can provide useful information regarding the thermodynamic and kinetics of sodium intercalation reactions, which indeed determine the shapes of the voltammograms. As an example, the voltammograms of Fe-doped samples are reported in Figure 8, while in Figure S5 in the Supplementary Materials, those of all the other samples are shown.
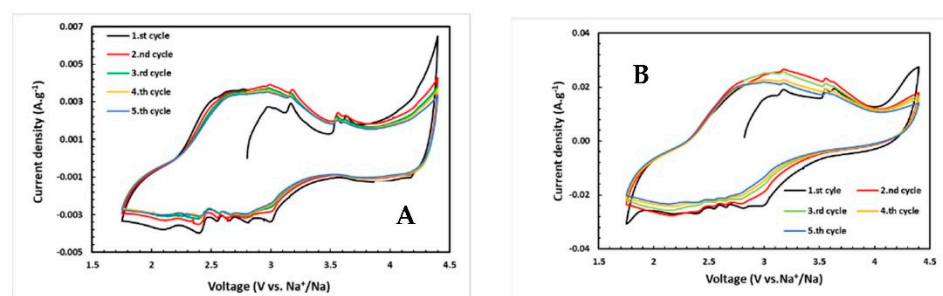

Figure 8. CV curves of (**A**) Fe02 and (**B**) Fe02-Q samples.

The voltammograms appeared quite different between the samples. In all the cases, many redox peaks can be observed, which were an indication of the multiple reactions taking place during sodium intercalation/deintercalation, due to the complex phase's stabilization and to the multiple reactions of the layered polymorphs. For these materials, the redox processes were expected to be mainly due to Mn ions [9,12,31,32]. The most defined phenomena can be observed for the NMO sample (Figure S5A in the Supplementary Materials). The oxidation peak at about 2.45 V was due to the Mn^{3+}/Mn^{4+} redox couple [33]. In the reduction step, the lower intensity of the peak suggested the partial irreversibility of the phenomenon because some Mn ions can maintain the 4+ oxidation state. The peak at 4.39 V can be ascribed to the P2-O2 phase transition, which is considered detrimental to capacity retention: by setting the cutoff voltage to 4 V, this phenomenon could be avoided at the expense of some capacity loss [13]. The multiple pairs of the small redox peaks below 3 V were attributed to the structural rearrangement of the layers, while the other small events between 3 and 4 V may be due to Na^+ vacancy ordering [12]. During cycling, the peak intensity decreased, suggesting a certain degree of irreversibility of the involved processes. It is also clearly evident that the oxidation peak attributed to Mn^{3+}/Mn^{4+} shifted to a higher potential from the first to the fifth cycle, suggesting the need for a higher driving force to extract sodium from the host, probably due to the structural changes of the layered material. The CV of the Cu02 sample (Figure S5C) was different from that of NMO, but in line with other Cu doped layered samples [34]: the main peaks located at 4.04V/3.81 V could be attributed to the Cu^{2+}/Cu^{3+} redox couple [14], presenting a small polarization and a good kinetics. The Mn^{3+}/Mn^{4+} redox peak at about 2.45 V, clearly evident in NMO, is now very low and broad. The other redox events can again be explained by sodium vacancy ordering. Apart from the first cycle, the CV curves were over-imposable, suggesting the good reversibility of the phenomena. The peak due to P2-O2 transition is lacking, as well as in Fe02 (Figure 8), suggesting the possible dopant efficacy to improve the cyclability, due to the decrease in the P2 amount, as demonstrated via XRPD (Table 1). The CV of the Fe02 sample showed many redox events in the oxidation range of 3–4 V and, in the cathodic scan, between 2 and 3 V. These can be attributed to the iron contribution (Fe^{3+}/Fe^{4+}) and to the layer's rearrangement/gliding. The CV curves of the quenched samples were quite different from their slow-cooled analogs (Figures 8 and S5). The NMO-Q showed flat curves without

clear evidence of redox phenomena. This may be due to the absence of the P2 phase and the presence of the main *Cmcm* phase, which is more structurally distorted. The CV of the Cu02-Q showed narrower peaks with a more defined Mn^{3+}/Mn^{4+} oxidation phenomenon, without polarization, showing some similarity with Cu02. The same is true for the Fe02-Q voltammograms, which are broader than those of Fe02 but with redox events again being recognizable.

The rate capability tests for slowly cooled and quenched samples are reported in Figure 9A,B, respectively.
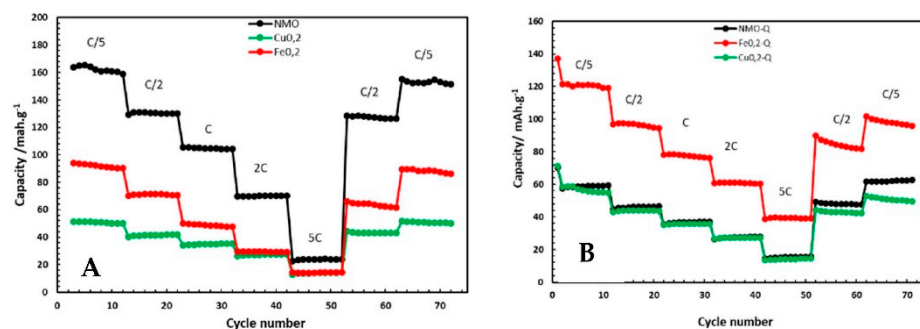

Figure 9. Discharge capacity values for slowly cooled (**A**) and quenched (**B**) samples.

For the slowly cooled samples, NMO showed the best performance, outperforming the doped samples at every C-rate. At C/5, capacity values of about 162 mAh/g were detected and at 2C values of about 70 mAh/g were again recorded. Fe02 had good performances, with a discharge capacity of about 92 mAh/g at C/5: its values were in line with those of similar materials reported in the literature [10,35]. Cu02 had instead capacity values of about 1/3 those of NMO (about 50 mAh/g at C/5), while maintaining good stability with an increase in the C-rate. In all the cases, the materials recover their initial capacities by returning to C/5, suggesting good reversibility. The performances of the quenched samples were different: the best results were provided by the Fe02-Q sample, with an initial discharge capacity of about 120 mAh/g at C/5 that decreased to 60 mAh/g at 2C. NMO-Q and Cu02-Q had similar capacities at all the C-rates, with values analogous to those of Cu02.

4. Discussion

The $Na_{0.67}MnO_2$ cathode material is currently attracting attention for its application in SIBs, mainly due to the high capacity and structural stability of the P2 phase, the main stable polymorph for this sodium composition. The wide range of possible cationic substitutions further allows for improving its functional properties. However, to develop electrochemically performing manganese-based P2 cathode materials, the elemental substitution necessitates the control of the Mn oxidation state. We achieved this goal by the combined use of structural and spectroscopic techniques.

Cu- and Fe-doped $Na_{0.67}MnO_2$ samples were successfully synthesized as mixtures of phases [31,32] due to the low temperature of thermal treatment, 800 °C, that was intentionally chosen to verify if the stabilization of the polymorph mixtures could allow to reach higher capacities or achieve better cycling stability, thanks to the favorable cushioning of structural transitions [7,11,36].

As previously demonstrated by XRPD, P2 and P'2 were the main phases for all the samples, apart from NMO-Q. This is in line with the literature findings on $Na_{0.67}Mn_{1-x}Mg_xO_2$ [11], in which the quenching process favors, as in our case, *Cmcm* stabilization for undoped and slightly doped samples, apart from x = 0.2, the same doping level used in the present work, for which the P2 phase is instead stabilized. In our case, in fact, the doping always allowed the stabilization of the P2 hexagonal polymorph as the main phase, independently of the cooling treatment, even if the amount of the P'2 phase

increased in the quenched samples. This observation, based on the XRPD evidence (Table 1), was also consistent with the EPR results. In fact, the P'2 phase is stabilized when a low number of Mn vacancies is formed, with a consequent reduction in the amount of Mn^{4+} ions, which are, therefore, preferentially surrounded by Mn^{3+} ions, thereby giving rise to broad EPR lines with g-values that are generally far from the ideal 1.996 value, which is typical of samples with Mn^{4+} as the unique magnetic ion. For slowly cooled samples, the EPR spectra of the Cu-doped samples showed a lower intensity with respect to pure and Fe-doped samples. This evidence suggests a complex behavior that cannot be explained only on the basis of the possible variation of manganese oxidation states as a consequence of the dopant introduction or quenching treatment [11].

O-type polymorphs were also present (Table 1), apart from the Cu02 sample, which only contained P-type polymorphs. The intergrowth of the P- and O-type phases is not new for layered cathodes: similar composites were obtained experimentally but were also simulated by structure modeling to calculate the diffraction patterns, to be compared with the complex experimental patterns [27,31,32,37]. For slowly cooled samples, the O polymorphs' amount is similar for NMO and Fe02, while the presence of Cu ions suppresses the gliding of planes, avoiding the segregation of O-type phases. For the quenched samples, the O-type phases are present in all the samples in a higher amount for NMO-Q, demonstrating that the cooling treatment is a prevailing factor with respect to doping.

We demonstrated that iron and copper can easily substitute for manganese on the octahedral sites of the layers, as suggested by the absence of phases only containing the dopant ions and by the changes in lattice parameters with respect to undoped NMO, which was particularly evident in the quenched samples. The Mössbauer data suggested that iron ions were present in both the P-type polymorphs, with a preference for the more regular octahedral sites of the P2 structure. The distribution of the dopants in both the structures can be predicted by the unit cell volume of P2 and P'2: after doping, they are about 2–3% and 4–6% higher with respect to the undoped sample. For the main P2 phase, both the *a* and *c* crystallographic axes increased (Table 1). The enlargement of the *c*-axis could, in principle, be useful for an easy Na^+ insertion/extraction during cell functioning, but, at the same time, it could favor the instability of the electrode structure [33]. The increase in the *a*-axis instead weakens the repulsion in the transition metal layers and, during structure changes upon cycling, particularly at high voltage, the long-range structure can change and the distortion effect will begin to have an impact on the structural reversibility, which can lead to poor capacity retention and rate performance. This scenario seems to suggest that, from the structural point of view, the dopant ions could have an unfavorable influence on the electrochemical properties. The lattice parameter variations can be attributed to the differences in the ionic radii of the stabilized species in octahedral coordination, Mn^{3+}/Mn^{4+} (suggested by the EPR spectra analysis), and Cu^{2+} and Fe^{3+} ions (as determined by Mössbauer spectroscopy) [38]. This is particularly true for the quenched samples, where no Mn vacancies should be present.

The crystallite sizes of the P2 phase were about twice those of the P'2 phase, for all the synthesized samples, independently of the cooling treatment. This is in line with the higher structural order degree of the P2 polymorph with respect to P'2, as is consistent with the line width of the relative EPR contributions. In particular, the copper ions heavily affected the crystallite size values, which are bigger than those of the pure and iron-doped samples for both the polymorphs (Table 1), as well as the external morphology of the particles, with micron-sized dimensions and without clear platelet particles. The morphology of the samples also changed, passing from the slowly cooled to the quenched samples: the rapid cooling maintained the grains' aggregation, which could be the basis of the worsening of electrochemical performances. It is well known that the downsizing of the grains, decreasing the diffusion paths, favors the Na^+ migration. In particular, the unfavorable morphology could justify the worst performances of the Cu-doped slowly cooled and quenched samples, (Figure 9). The marked influence of the dopant ions was

evident in terms of the structural stability as a function of time. The undoped sample had good stability for at least 7–14 days. This is due to the intrinsic characteristics of the P2 polymorph, considered one of the most stable between the P- and O-type layered phases, but this is also valid for *Cmcm*, the main phase of the NMO-Q sample. The introduction of iron does not markedly change the behavior of NMO: only in the case of Fe02-Q, after 30 days, high degradation was evident, with a concomitant loss of crystallinity of the main P2 phase. The copper substitution, instead, helped to improve the stability because the formed phases remained practically unchanged for up to 30 days. This evidence is in agreement with the literature findings, suggesting copper substitution as a way to enhance the stability of layered electrode materials [14].

We could try to relate the electrochemical performances (Figures 8, 9, and S5) to the structural and morphological peculiarities of the samples. The CV curves were complex, with multiple events, due to the presence of complex mixtures of phases that were electrochemically active. The NMO sample, with the highest amount of P2 phase, had a well-defined CV, in which the redox peak of Mn^{3+}/Mn^{4+} couple and the peak at about 4.39 V, due to P2-O2 transformation, can be recognized. However, the peak intensities decreased, and the positions shifted to higher potential in the anodic scan, passing from the first to the fifth cycle. These effects could be related to the marked structural changes occurring during cycling. The introduction of dopants limited the intensity decrease during cycling: both the doped samples have better reversibility. This may be due to the coexistence of a higher amount of structurally different phases. In fact, the doping and the quenching caused the increase in P'2 polymorph amount, as well as O-type phases, particularly in the quenched samples. The Fe-doped samples and, partly, the Cu samples (at least at lower potentials) had broader peaks, suggesting that the electrochemical phenomena occurred in a wide potential window, due to the increase in the amount of distorted polymorphs. These observations were in agreement with the line-broadening of EPR spectra.

In the slowly cooled samples, the NMO had the highest capacity values (about 162 mAh/g); however, these rapidly decreased by increasing the C-rates, even if the capacity at 2C was again acceptable. A similar trend was verified by Guo et al. [37] on layered $Na_{0.66}Li_{0.18}Mn_{0.71}Ni_{0.21}Co_{0.08}O_{2+\delta}$ P2/O3 composite. The minor presence of the O3 phase, together with the main P2 phase, is responsible for the satisfactory rate capability. The O3 phase can supply more sodium ions, while the enlarged layered spacings of the P2 phase are beneficial for the easy diffusion of sodium ions upon the charging process. A good rate capability is shown by the Fe02 sample, also having some amount of O3 Na+ reservoir phase, but in this case, the enlargement of the lattice parameters of P2 phase and the stabilization of a larger amount of P'2 polymorph seem to negatively influence the electrochemical performance. Cu02 has the worst performance, although with a lower decrease in capacity during cycling at an increasing C-rate. The Cu-doped samples' poor performance may mainly be due to the kinetic limitations related to the higher diffusion paths of sodium, because of the larger particle sizes, and due to the absence of O-type phases. So the NMO, containing a higher amount of P2 with respect to Fe02 and Cu02 and with smaller lattice parameters, could better buffer the structural changes during cycling. In some papers, it has been suggested that both the Cu^{2+} and Fe^{3+} in the P2 phase are active redox couples providing themselves a contribution to the overall capacity [14,21]. In fact, from the CV data of the Cu-doped samples (Figure S5), the peak at about 4 V can be attributed to the Cu^{2+}/Cu^{3+} redox couple [14]. Despite the possible dopant contribution to the capacity, in the slowly cooled samples, the prevailing factor on the capacity values is the P2 phase prevalence, together with a small amount of O-type phases (particularly O3). The effect of dopant, as demonstrated by the EPR measurements, is different from what was expected. In fact, particularly in the case of the Cu-doped samples, the amount of Mn^{4+} did not increase, as demonstrated by the decrease in EPR signal intensity with respect to NMO (Figure 4), suggesting a possible decrease in oxygen absorption and, in turn, a lower number of manganese vacancies with respect to NMO. This evidence could

also help to explain the poor electrochemical capacities. The performance of the quenched samples was lower with respect to the slowly cooled samples. The reason for this difference could be due to the different morphologies and to the different stabilizations of the phases. In fact, NMO-Q (Figure 2) presented particles that seemed to melt together, forming large aggregates, which was different from NMO. In addition, the main phase of this sample was the *Cmcm* polymorph, with a more distorted structure, limiting easy Na+ diffusion. In addition, a high percentage of O-type phases was stabilized, which may have worsened the electrochemical performance. In fact, the intervention of intermediate sites in the sodium migration needs to overcome a high-energy barrier for the O3-type structure; the inevitable complex phase transition and weak kinetics performance will directly influence the electrochemical properties. Only Fe02-Q, with a low degree of agglomeration and a low percentage of O-type polymorphs, together with the P2 phase as the main phase (similarly to NMO) with respect to NMO-Q, has a satisfying rate capability (Figure 9). It also demonstrated high capacity values at higher C-rates with respect to NMO, and a less pronounced capacity decrease by increasing the C-rates. The Cu-doped sample also yields the worst performances, due to the same reasons previously given for Cu02. In the case of the quenched samples, however, the P2 amount was further decreased in the doped samples and, from the broad EPR signals, we could hypothesize a high value for the Mn^{3+}/Mn^{4+} ratio, as also indicated by the EDS results (Table 2), which can also justify the limited electrochemical results.

The deepening of the electrochemical results by performing long-cycling measurements in the search for the most competitive samples or ex situ XRPD measurements, to better clarify the mechanisms of Na storage, were outside the aim of the present work and will be the subject of future work, starting from these preliminary results and working on optimized samples.

5. Conclusions

We synthesized undoped and Cu- or Fe-doped $Na_{0.67}MnO_2$ samples, with two different cooling steps to room temperature, either in a natural way or by quenching. The use of a combination of characterization techniques, mainly with structural and spectroscopic methods, allowed us to demonstrate the complex nature of the samples, as constituted by mixtures of polymorphs. Thanks to these results, the preliminary cyclic voltammetry, and galvanostatic cycling results were interpreted: the introduction of substituents, in general, seems to worsen the capacity values (apart from the Fe02-Q sample, which had satisfactory capacity values), mainly due to the decrease in the P2 amount, higher diffusion paths for sodium, and the maintenance in the samples of a high amount of Mn^{3+}. We demonstrated, once again, the need to deepen the physico-chemical features of electrode materials to fully understand electrochemical performance for the design of new and outstanding cathodes for SIBs.

Author Contributions: Investigation: M.A., M.S., M.F., A.C. and M.C.M.; methodology: M.A.; visualization: M.A. and I.Q.; review and editing: D.S., M.S., A.C., M.F. and M.C.M.; writing—original draft: M.B., M.C.M., M.F. and A.C.; supervision: M.B. All authors have read and agreed to the published version of the manuscript.

to the Project "CE4WE—Circular economy for Water and Energy" funded by the Lombardy Region (1139857 CALL HUB 2018).

References

1. Yabuuchi, N.; Kubota, K.; Dahbi, M.; Komaba, S. Research Development on Sodium-Ion Batteries. *Chem. Rev.* **2014**, *114*, 11636−11682. https://doi.org/10.1021/cr500192f.
2. Li, L.; Zheng, Y.; Zhang, S.; Yang, J.; Shao, Z.; Guo, Z. Recent progress on sodium ion batteries: Potential high-performance anodes. *Energy Environ. Sci.* **2018**, *11*, 2310–2340. https://doi.org/10.1039/C8EE01023D.
3. Lv, W.J.; Huang, Z.; Yin, Y.X.; Yao, H.R.; Zhu, H.L.; Guo, Y.G. Strategies to Build High-Rate Cathode Materials for Na-Ion Batteries. *ChemNanoMat* **2019**, *5*, 1253–1262. https://doi.org/10.1002/cnma.201900254.
4. Sun, Y.; Guo, S.; Zhou, H. Exploration of Advanced Electrode Materials for Rechargeable Sodium-Ion Batteries. *Adv. Energy Mater.* **2019**, *9*, 1800212. https://doi.org/10.1002/aenm.201800212.
5. Liu, Q.; Hu, Z.; Chen, M.; Zou, C.; Jin, H.; Wang, S.; Chou, S.L.; Dou, S.X. Recent Progress of Layered Transition Metal Oxide Cathodes for Sodium-Ion Batteries. *Small* **2019**, *15*, 1805381. https://doi.org/10.1002/smll.201805381.
6. Delmas, C.; Fouassier, C.; Hagenmuller, P. Structural classification and properties of the layered oxides. *Phys. B* **1980**, *99*, 81–85. https://doi.org/10.1016/0378-4363(80)90214-4.
7. Kumakura, S.; Tahara, Y.; Kubota, K.; Chihara, K.; Komaba, S. Sodium and Manganese Stoichiometry of P2-Type $Na_{2/3}MnO_2$. *Angew. Chem. Int. Ed.* **2016**, *55*, 12760–12763. https://doi.org/10.1002/anie.201606415.
8. Lee, D.H.; Xu, J.; Meng, Y.S. An advanced cathode for Na-ion batteries with high rate and excellent structural stability. *Phys. Chem. Chem. Phys.* **2013**, *15*, 3304–3312. https://doi.org/10.1039/C2CP44467D.
9. Peng, B.; Sun, Z.; Jiao, S.; Wang, G.; Zhang, G. Electrochemical Performance Optimization of Layered P2-Type Na0.67MnO2 through Simultaneous Mn-Site Doping and Nanostructure Engineering. *Batter. Supercaps* **2020**, *3*, 147–154. https://doi.org/10.1002/batt.201900126.
10. Liu, X.; Zhong, G.; Xiao, Z.; Zheng, B.; Zuo, W.; Zhou, K.; Liu, H.; Liang, Z.; Xiang, Y.; Chen, Z.; et al. Al and Fe-containing Mn-based layered cathode with controlled vacancies for high-rate sodium ion batteries. *Nano Energy* **2020**, *76*, 104997. https://doi.org/10.1016/j.nanoen.2020.104997.
11. Billaud, J.; Singh, G.; Armstrong, A.R.; Gonzalo, E.; Roddatis, V.; Armand, M.; Rojo, T.; Bruce, P.G. Na0.67Mn1-xMgxO2 (0 < x < 0.2): A high capacity cathode for sodium-ion batteries. *Energy Environ. Sci.* **2014**, *7*, 1387–1391. https://doi.org/10.1039/c4ee00465e.
12. Hemalatha, K.; Jayakumar, M.; Prakash, A.S. Influence of the manganese and cobalt content on the electrochemical performance of P2-Na0.67MnxCo1−xO2 cathodes for sodium-ion batteries. *Dalton Trans.* **2018**, *47*, 1223–1232. https://doi.org/10.1039/C7DT04372D.
13. Zuo, W.; Qiu, J.; Liu, X.; Zheng, B.; Zhao, Y.; Li, J.; He, H.; Zhou, K.; Xiao, Z.; Li, Q.; et al. Highly-stable P2–Na0.67MnO2 electrode enabled by lattice tailoring and surface engineering. *Energy Storage Mater.* **2020**, *26*, 503–512. https://doi.org/10.1016/j.ensm.2019.11.024.
14. Li, Y.; Yang, Z.; Xu, S.; Mu, L.; Gu, L.; Hu, Y.S.; Li, H.; Chen, L. Air-Stable Copper-Based P2-Na7/9Cu2/9Fe1/9Mn2/3O2 as a New Positive Electrode Material for Sodium-Ion Batteries. *Adv. Sci.* **2015**, *2*, 1500031. https://doi.org/10.1002/advs.201500031.
15. Kang, W.; Yu, D.Y.W.; Lee, P.K.; Zhang, Z.; Bian, H.; Li, W.; Ng, T.E.; Zhang, W.; Lee, C.S. P2-Type NaxCu0.15Ni0.20Mn0.65O2 Cathodes with High Voltage for High-Power and Long-Life Sodium-Ion Batteries. *ACS Appl. Mater. Interfaces* **2016**, *8*, 31661−31668. https://doi.org/10.1021/acsami.6b10841.
16. Zhang, Y.; Xia, X.; Liu, B.; Deng, S.; Xie, D.; Liu, Q.; Wang, Y.; Wu, J.; Wang, X.; Tu, J. Multiscale Graphene-Based Materials for Applications in Sodium Ion Batteries. *Adv. Energy Mater.* **2019**, *9*, 1803342. https://doi.org/10.1002/aenm.201803342.
17. Zhang, L.L.; Wei, C.; Fu, X.Y.; Chen, Z.Y.; Yan, B.; Sun, P.P.; Chang, K.J.; Yang, X.L. Ternary Ni-based Prussian blue analogue with superior sodium storage performance induced by synergistic effect of Co and Fe. *Carbon Energy* **2021**, *3*, 827–839. https://doi.org/10.1002/cey2.142.
18. Li, Y.; Chen, M.; Liu, B.; Zhang, Y.; Liang, X.; Xia, X. Heteroatom Doping: An Effective Way to Boost Sodium Ion Storage. *Adv. Energy Mater.* **2020**, *10*, 2000927. https://doi.org/10.1002/aenm.202000927.
19. Parant, J.P.; Olazcuaga, R.; Devalette, M.; Fouassier, C.; Hagenmuller, P. Sur quelques nouvelles phases de formule $NaxMnO_2$ (x ⩽ 1). *J. Solid State Chem.* **1971**, *3*, 1–11. https://doi.org/10.1016/0022-4596(71)90001-6.
20. Mason, C.W.; Lange, F.; Saravanan, K.; Lin, F.; Nordlund, D. Beyond Divalent Copper: A Redox Couple for Sodium Ion Battery Cathode Materials. *ECS Electrochem. Lett.* **2015**, *4*, A41-A44. https://doi.org/10.1149/2.0041505eel.

21. Darbar, D.; Muralidharan, N.; Hermann, R.P.; Nanda, J.; Bhattacharya, I. Evaluation of electrochemical performance and redox activity of Fe in Ti doped layered P2-Na 0.67 Mn 0.5 Fe 0.5 O 2 cathode for sodium ion batteries. *Electrochim. Acta* **2021**, *380*, 138156. https://doi.org/10.1016/j.electacta.2021.138156.

22. Bruker AXS. *TOPAS V3.0: General Profile and Structural Analysis Software for Powder Diffraction Data*; User Manual Bruker AXS: Karlsruhe, Germany, 2005.

23. Spina, G.; Lantieri, M. A Straightforward Experimental Method to Evaluate the Lamb-Mössbauer Factor of a 57Co/Rh Source. *Nucl. Instruments Methods Phys. Res. Sect. B Beam Interact. Mater. Atoms* **2014**, *318*, 253–257. https://doi.org/10.1016/j.nimb.2013.10.002.

24. Chen, L.; De-ping, Y. *Mössbauer Effect in Lattice Dynamics: Experimental Techniques and Applications*; WILEY-VCH Verlag GmbH & Co. KGaA: Weinheim, Germany, 2007; ISBN 978-3.527-40712-5.

25. Bini, M.; Ferrari, S.; Capsoni, D.; Mustarelli, P.; Spina, G.; Del Giallo, F.; Lantieri, M.; Leonelli, C.; Rizzuti, A.; Massarotti, V. Pair distribution function analysis and Mössbauer study of defects in microwave-hydrothermal $LiFePO_4$. *RSC Adv.* **2012**, *2*, 250–258. https://doi.org/10.1039/C1RA00525A.

26. Stoyanova, R.; Carlier, D.; Sendova-Vassileva, M.; Yoncheva, M.; Zhecheva, E.; Nihtianova, D.; Delmas, C. Stabilization of over-stoichiometric Mn^{4+} in layered $Na_{2/3}MnO_2$. *J. Solid State Chem.* **2010**, *183*, 1372–1379. https://doi.org/10.1016/j.jssc.2010.04.024.

27. Sathiya, M.; Jacquet, Q.; Doublet, M.L.; Karakulina, O.M.; Hadermann, J.; Tarascon, J.M. A Chemical Approach to Raise Cell Voltage and Suppress Phase Transition in O3 Sodium Layered Oxide Electrodes. *Adv. Energy Mater.* **2018**, *8*, 1702599. https://doi.org/10.1002/aenm.201702599.

28. Gutlich, P.; Eckhard, B.; Trautwein, A.X. *Mössbauer Spectroscopy and Transition Metal Chemistry: Fundamentals and Applications*; Springer: Berlin/Heidelberg, Germany, 2011.

29. Talaie, E.; Duffort, V.; Smith, H.L.; Fultz, B.; Nazar, L.F. Structure of the high voltage phase of layered P2-Na2/3-z[Mn1/2Fe1/2]O2 and the positive effect of Ni substitution on its stability. *Energy Environ. Sci.* **2015**, *8*, 2512–2523. https://doi.org/10.1039/C5EE01365H.

30. Massarotti, V.; Capsoni, D.; Bini, M.; Azzoni, C.B.; Paleari, A. Stoichiometry of Li2MnO3and LiMn2O4Coexisting Phases: XRD and EPR Characterization. *J. Solid State Chem.* **1997**, *128*, 80–86. https://doi.org/10.1006/jssc.1996.7158.

31. Nuti, M.; Spada, D.; Quinzeni, I.; Capelli, S.; Albini, B.; Galinetto, P.; Bini, M. From tunnel NMO to layered polymorphs oxides for sodium ion batteries. *SN Appl. Sci.* **2020**, *2*, 1893. https://doi.org/10.1007/s42452-020-03607-z.

32. Leccardi, F.; Nodari, D.; Spada, D.; Ambrosetti, M.; Bini, M. Synergistic Effect of Polymorphs in Doped NaNi0.5Mn0.5O2 Cathode Material for Improving Electrochemical Performances in Na-Batteries. *Electrochem* **2021**, *2*, 335–346. https://doi.org/10.3390/electrochem2020024.

33. Luo, R.; Zhang, N.; Wang, J.; Qu, W.; Li, L.; Wu, F.; Chen, R.J. Insight into effects of divalent cation substitution stabilizing P2-Type layered cathode materials for sodium-ion batteries. *Electrochim. Acta* **2021**, *368*, 137614. https://doi.org/10.1016/j.electacta.2020.137614.

34. Yin, X.S.; Yan, W.X.; Ming, L.Y.; Sheng, H.Y.; Quan, C.L. Novel copper redox-based cathode materials for room-temperature sodium-ion batteries. *Chin. Phys. B* **2014**, *23*, 118202. https://doi.org/10.1088/1674-1056/23/11/118202.

35. Luo, C.; Langrock, A.; Fan, X.; Liangand, Y.; Wang, C. P2-type transition metal oxides for high performance Na-ion battery cathodes. *J. Mater. Chem. A* **2017**, *5*, 18214–18220. https://doi.org/10.1039/C7TA04515H.

36. Yabuuchi, N.; Hara, R.; Kajiyama, M.; Kubota, K.; Ishigaki, T.; Hoshikawa, A.; Komaba, S. New O2/P2-type Li-Excess Layered Manganese Oxides as Promising Multi-Functional Electrode Materials for Rechargeable Li/Na Batteries. *Adv. Energy Mater.* **2014**, *4*, 1301453. https://doi.org/10.1002/aenm.201301453.

37. Guo, S.; Liu, P.; Yu, H.; Zhu, Y.; Chen, M.; Ishida, M.; Zhou, H. A Layered P2- and O3-Type Composite as a High-Energy Cathode for Rechargeable Sodium-Ion Batteries. *Angew. Chem. Int. Ed.* **2015**, *54*, 5894–5899. https://doi.org/10.1002/anie.201411788.

38. Shannon, R.D. Revised effective ionic radii and systematic studies of interatomic distances in halides and chalcogenides. *Acta Crystallogr.* **1976**, *32*, 751–767. https://doi.org/10.1107/S0567739476001551.